Geometrical effects on the concentrated behavior of heat flux in metamaterials thermal harvesting devices

Cite as: AIP Advances **7**, 105322 (2017); https://doi.org/10.1063/1.4986984
Submitted: 07 June 2017 . Accepted: 19 October 2017 . Published Online: 30 October 2017

Guoqiang Xu, Haochun Zhang, Ming Xie, and Yan Jin

AIP ADVANCES **7**, 105322 (2017)

Geometrical effects on the concentrated behavior of heat flux in metamaterials thermal harvesting devices

Guoqiang Xu,[1] Haochun Zhang,[1,a] Ming Xie,[1] and Yan Jin[2]
[1]*School of Energy Science and Engineering, Harbin Institute of Technology, Harbin 150001, China*
[2]*Institute of Thermo-Fluid Dynamics, Hamburg University of Technology, Hamburg D 21073, Germany*

(Received 7 June 2017; accepted 19 October 2017; published online 30 October 2017)

Thermal harvesting devices based on transformation optics, which can manipulate the heat flux concentration significantly through rational arrangements of the conductivities, have attracted considerable interest owing to several great potential applications of the technique for high-efficiency thermal conversion and collection. However, quantitative studies on the geometrical effects, particularly wedge angles, on the harvesting behaviors are rare. In this paper, we adopt wedge structure-based thermal harvesting schemes, and focus on the effects of the geometrical parameters including the radii ratios and wedge angles on the harvesting performance. The temperature deformations at the boundaries of the compressional region and temperature gradients for the different schemes with varying design parameters are investigated. Moreover, a concept for temperature stabilization was derived to evaluate the fluctuation in the energy distributions. In addition, the effects of interface thermal resistances have been investigated. Considering the changes in the radii ratios and wedge angles, we proposed a modification of the harvesting efficiency to quantitatively assess the concentration performance, which was verified through random tests and previously fabricated devices. In general, this study indicates that a smaller radii ratio contributes to a better harvesting behavior, but causes larger perturbations in the thermal profiles owing to a larger heat loss. We also find that a smaller wedge angle is beneficial to ensuring a higher concentration efficiency with less energy perturbations. These findings can be used to guide the improvement of a thermal concentrator with a high efficiency in reference to its potential applications as novel heat storage, thermal sensors, solar cells, and thermoelectric devices. https://doi.org/10.1063/1.4986984

I. INTRODUCTION

The use of transformation optics[1] (TO) for active management and regulation of physical fields, including optics,[2,3] electromagnetism,[4] acoustics,[5] and elasticity,[6] was a research focus because of its significant impact on both fundamental researches and engineering applications. The form invariance of the heat diffusion equation after coordinate transformation led to the extension of TO to the thermal field to guide the design and experiments of thermal TO devices including thermal cloaks,[7–13] concentrators,[14–25] rotators,[26] camouflage,[27] and diodes.[28] With thermal TO devices, an active and efficient control of thermal energy can be achieved with a pre-designed profile and reasonable arrangement of metamaterials.

Among the novel thermal TO devices, the development of metamaterials-based thermal harvesting devices utilized to concentrate the heat flux was rapid in recent years owing to their significant applications in improving the technique and efficiency of thermal collectors for thermoelectricity,[29]

[a]Corresponding author. E-mail address: zhc7@vip.163.con (H. C. Zhang).

solar collectors,[30] heat storage[31] and fuel cells.[32] Based on the coordinate transformation of Maxwell equations,[1–4] transformation thermodynamics,[14] aimed at mapping material parameters onto the transformational domain, was proposed to manipulate the heat flux, and the components of the anisotropic conductivities for both thermal cloaks and concentrators were observed using the Jacobian matrix. To realize local heat harvesting, alternative composite materials with a wedge-like structure (e.g., spoke, fan, and sensu) were widely adopted in previous studies.[14–19,21–23] The feasible method for fabricating a thermal concentrator is reversing the conductivity components[15] in the transformational domain, i.e., keeping the radial component considerably larger than the azimuthal component. Based on this concept, theoretical 3D thermal harvesting cells[16] have been demonstrated by employing naturally available materials with tunable anisotropy. Furthermore, the harvesting efficiency was proposed as a parameter to evaluate the concentration behavior, and a nearly 100% efficiency was determined with the theoretical 3D scheme. In addition, a 2D harvesting scheme with easily fabricated metamaterials[17] was designed and experimentally achieved, leading to a drastic increase in the temperature gradient in the central region of the entire model. The control of thermal conduction,[18] including focus, resolving, and uniform heating, can be flexibly achieved by adopting relevant metamaterial-based multiple wedge cells and rationally regulating their arrangement. Furthermore, a type of dual-function thermal metamaterial was proposed by employing homogeneous isotropic materials and shape-memory alloys for realizing automatic switching between a thermal cloak and concentrator.[19] In recent years, TO-based thermal harvesting devices were extended to attain convergent heat transfer[33] via rotation and compression transformations, to design multifunctional metamaterials,[20–23] which manipulated Laplace fields (thermal and electric)[22] simultaneously, and to fabricate tunable unit-cell thermal shifters[34] by considering the heat flux bending[35,36] in the material layers. To concentrate the heat flux more effectively, the influence of conductivities[24] was investigated, and it showed that a larger conductivity ratio of the radial and azimuthal components ensured a better harvesting performance. Additionally, an optimization algorithm[34] was proposed to minimize the error in the distributions of the conductivities to enhance the harvesting performance. However, the conductivity ratio can barely approach the ideal value owing to the limitations of the actual applications. Thus, exploring the effects of geometry on the harvesting behavior is highly desirable to maximally intensify the actual wedge-structure concentration efficiency. In this paper, we focused on quantitatively investigating the geometrical influences, including those of radii ratios and wedge angles, on the harvesting behavior through a rigorous theoretical analysis, and several harvesting schemes with varying geometrical parameters were established. Considering the energy loss in wedge structure schemes, temperature stabilization was observed to evaluate the fluctuation in the energy distributions in the thermal compressional region. Finally, we proposed a modification of the harvesting efficiency by considering the geometrical effects and verified its accuracy and effectiveness through random tests and previous fabricated devices.[17,18,21,34]

II. GEOMETRICAL PROFILE AND THEORETICAL ANALYSIS

The heat transfer process for such thermal harvesting devices[11–23] can be presented by the rigorous theoretical model[8,9,16,24] as shown in Fig. 1.

By employing the Jacobian matrix,[14] the thermal conductivities in the radial and azimuthal components for a 2D harvesting scheme, as illustrated in Fig. 1a, can be deduced.

$$\kappa_r = \frac{\omega r}{r'} = \kappa_0 + \frac{R_2}{r'}\left(\frac{R_0 - R_1}{R_2 - R_0}\right)\kappa_0, \tag{1a}$$

$$\kappa_\theta = \frac{r'}{\omega r} = \frac{\kappa_0}{1 + \frac{R_2}{r'}\left(\frac{R_0 - R_1}{R_2 - R_0}\right)}, \tag{1b}$$

where, R_2 is the outer radial, R_0 and R_1 respectively denote the inner radii in the original and transformational domains, r' is the radial position of any points in the range of $R_1 \sim R_2$ in transformation domain, and r is the corresponding points in the range of $R_0 \sim R_2$ of the original domain. $\omega = (R_2 - R_1)/(R_2 - R_0)$ denotes the degree of compression in the radial direction corresponding to the coordinate transformation. κ_0 is the thermal conductivity of the surrounding. The profile of a thermal

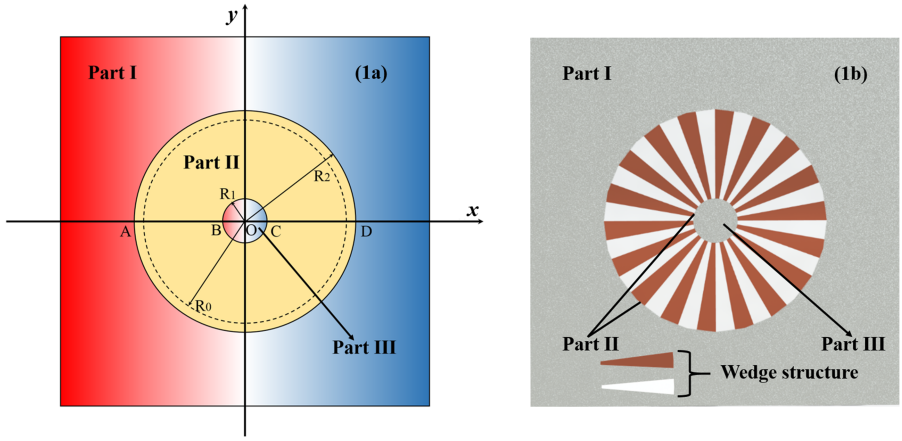

FIG. 1. Models for thermal harvesting schemes: a. Schematic of the metamaterial thermal concentrator; b. Actual thermal harvesting scheme with wedge structure used for realize thermal compression.

harvesting device[14–25] based on a spatial transformation can be separated into three parts including the background (Part I), concentrating region (Part II), and central region (Part III). In this view, heat transfer properties in the entire system can be deduced by rigorously solving the conduction function of the three parts under certain boundary conditions. Thus, for a 2D thermal harvesting scheme without a source, the heat diffusion in Part II can be written as:

$$\rho' c' \frac{\partial T}{\partial t} = \frac{1}{r'} \frac{\partial}{\partial r'} \left(\kappa_r r' \frac{\partial T}{\partial r'} \right) + \frac{1}{(r')^2} \frac{\partial}{\partial \theta'} \left(\kappa_\theta \frac{\partial T}{\partial \theta'} \right), \tag{2}$$

Appling a constant temperature gradient along the x direction, Eq. (1) can be written as:

$$\frac{1}{r'} \frac{\partial}{\partial r'} \left(\kappa_r r' \frac{\partial T}{\partial r} \right) + \frac{1}{(r')^2} \frac{\partial}{\partial \theta'} \left(\kappa_\theta \frac{\partial T}{\partial \theta'} \right) = 0, \tag{3}$$

Dividing both the left and right sides by κ_r, we can obtain:

$$\frac{\partial^2 T}{\partial (r')^2} + \frac{1}{r'} \frac{\partial T}{\partial r'} + \frac{1}{(r')^2} \frac{\kappa_\theta}{\kappa_r} \frac{\partial}{\partial \theta'} \left(\frac{\partial T}{\partial \theta'} \right) = 0, \tag{4}$$

Here, we introduce a new variable ε to represent the ratio of the conductivities of the radial and azimuthal components, i.e. $\varepsilon = \kappa_\theta / \kappa_r = (r'R_2\text{-}r'R_0)^2 / (r'(R_2\text{-}R_0)+R_2\cdot(R_0\text{-}R_1))^2$. Considering the homogeneous materials in the regions of background and center, $\varepsilon = 1$. Hence, the temperature in the three parts can be deduced generally based on the symmetry that is centered on the x axis:[8]

$$T_{\mathrm{I}} = \sum_{m=1}^{\infty} \left(A_{2m-1} r^{2m-1} + B_{2m-1} r^{-2m+1} \right) \cos\left(2m-1\right)\theta, \tag{5a}$$

$$T_{\mathrm{II}} = \sum_{m=1}^{\infty} \left(C_{2m-1} r^{(2m-1)\sqrt{\varepsilon}} + D_{2m-1} r^{-(2m-1)\sqrt{\varepsilon}} \right) \cos\left(2m-1\right)\theta, \tag{5b}$$

$$T_{\mathrm{III}} = \sum_{m=1}^{\infty} \left(E_{2m-1} r^{2m-1} + F_{2m-1} r^{-2m+1} \right) \cos\left(2m-1\right)\theta, \tag{5c}$$

Considering the continuity of the heat flux vector between the interfaces of adjacent regions, the following relations can be established:

$$T_{\mathrm{I}}|_{r=R_2} = T_{\mathrm{II}}|_{r=R_2}, \; \kappa_0 \left. \frac{\partial T_{\mathrm{I}}}{\partial r} \right|_{r=R_2} = \kappa_r \left. \frac{\partial T_{\mathrm{II}}}{\partial r} \right|_{r=R_2}, \tag{6a}$$

$$T_{\mathrm{II}}|_{r=R_1} = T_{\mathrm{III}}|_{r=R_1}, \; \kappa_r \left. \frac{\partial T_{\mathrm{II}}}{\partial r} \right|_{r=R_1} = \kappa_0 \left. \frac{\partial T_{\mathrm{III}}}{\partial r} \right|_{r=R_1}, \tag{6b}$$

On account of the linear distributions of the temperature in Parts I and III, both $B_{2m\text{-}1}$ and $F_{2m\text{-}1}$ are 0, and we only need to consider $m = 1$.[16] With the constant boundary conditions of T_L and T_R, Eqs. (5a)–(5c) can be represented as:

$$T_I = \frac{T_L + T_R}{2} - \frac{r'(T_L - T_R)\cos\theta}{2x_0}, \tag{7a}$$

$$T_{II} = \frac{T_L + T_R}{2} - \frac{r'(T_L - T_R)\cos\theta}{2x_0}\left(\frac{r'}{R_2}\right)^{\sqrt{\varepsilon}-1}, \tag{7b}$$

$$T_{III} = \frac{T_L + T_R}{2} - \frac{r'(T_L - T_R)\cos\theta}{2x_0}\left(\frac{R_1}{R_2}\right)^{\sqrt{\varepsilon}-1}, \tag{7c}$$

Based on Eqs. (7a)–(7c), the ideal temperature at any positions can be observed. Consequently, the temperature at the test points of A, B, C, and D on the symmetry line can be expressed as:

$$T_A = \frac{T_L + T_R}{2} + \frac{R_2(T_L - T_R)}{2x_0}, \tag{8}$$

$$T_B = \frac{T_L + T_R}{2} + \frac{R_1(T_L - T_R)}{2x_0}\left(\frac{R_1}{R_2}\right)^{\sqrt{\varepsilon}-1}, \tag{9}$$

$$T_C = \frac{T_L + T_R}{2} - \frac{R_1(T_L - T_R)}{2x_0}\left(\frac{R_1}{R_2}\right)^{\sqrt{\varepsilon}-1}, \tag{10}$$

$$T_D = \frac{T_L + T_R}{2} - \frac{R_2(T_L - T_R)}{2x_0}, \tag{11}$$

As Refs. 16 and 17 pointed out, the thermal harvesting efficiency with anisotropic heat conductivity variance can be presented as:

$$\eta = \frac{|T_B - T_C|}{|T_A - T_D|} = \left(\frac{R_1}{R_2}\right)^{\sqrt{\varepsilon}}, \tag{12}$$

The above equation shows that the efficiency of the harvesting performance of an ideal scheme approaches 100% if ε is approximately 0, i.e., $\omega \to \infty$. However, the efficiency of a real system cannot be 100% because of the significant limitations in achieving anisotropic thermal conductivities and applying wedge-shaped[14–24] thermally expanding structures with several wedges. For the former, the thermal contact resistances of Part II because the application of effective medium theory[26] should be compensated, i.e., the thermal conductivities of the chosen materials should meet the requirement, i.e. $\kappa_A \cdot \kappa_B \sim \kappa_r \cdot \kappa_\theta = \kappa_0^2$. Hence, the conductivities in the radial and azimuthal components with corresponding filling fractions can be also achieved based on effective medium theory.

$$\kappa_r = \alpha_A \times \kappa_A + \alpha_B \times \kappa_B, \tag{13a}$$

$$\kappa_\theta = \frac{1}{\frac{\alpha_A}{\kappa_A} + \frac{\alpha_B}{\kappa_B}}, \tag{13b}$$

As such, $\sqrt{\varepsilon}$ can be written as $1/\sqrt{(\alpha_A^2 + \alpha_B^2)\frac{\kappa_A}{\kappa_B} + \alpha_A\alpha_B\left(1 + \left(\frac{\kappa_A}{\kappa_B}\right)^2\right)}$. Additionally, a higher anisotropy in Part II ensures a higher thermal harvesting efficiency as $\varepsilon \to \infty$. Thus, a sufficiently large κ_A/κ_B will lead to a better thermal harvesting behavior with a smaller thermal energy perturbation in the surrounding. However, κ_A/κ_B cannot be made infinity or large enough in real fabrications because of the limitations of material properties and costs.[18] In this view, the harvesting behavior can be controlled by regulating the geometrical parameters under a certain limit of κ_A/κ_B in practical applications.

To investigate the geometrical effects of the structural parameters including the ratio of the inner and outer radii and wedge angles in the fan structure, the filling material in Parts I and II was chosen as nickel steel (25% Ni) with a thermal conductivity $\kappa_0 = 13\ \mathrm{W{\cdot}m^{-1}{\cdot}K^{-1}}$, and the filling fraction of both materials A and B was 0.5. Copper with a conductivity of $398\ \mathrm{W{\cdot}m^{-1}{\cdot}K^{-1}}$ was selected as material A. Furthermore, a composite of 99.93% polydimethylsiloxane (PDMS) and 0.07% copper in terms of

fractional area, with a thermal conductivity 0.425 $W \cdot m^{-1} \cdot K^{-1}$ calculated based on the formula[7,10,11] $\kappa_B = f_{Cu}\kappa_{Cu} + f_{PDMS}\kappa_{PDMS}$, was used as material B, where, f denotes the area fractions. Considering the material characteristics of PDMS, it served as interfacial material under the condition of perfect combination.[36] As Refs. 37 and 38 pointed out, the interface thermal resistances are depended on the surface topography of materials and thermal contact resistances between adjacent interfaces. Under the consideration of perfect combination, the thermal contact resistances is 0 and the estimates of the interfacial resistance[36–38] can be expressed as:

$$\mathbf{R}_{\text{int}} = l_B/\kappa_B = \frac{\left(R_2{}^2 - R_1{}^2\right)\sin\frac{\alpha}{2}}{\kappa_B} = \frac{R_2{}^2\left(1 - n^2\right)\sin\frac{\alpha}{2}}{\kappa_B}, \tag{14}$$

where, $\mathbf{R}_{\text{int}}$ is the interfacial resistance of the composite layer, and l_B denotes the effective thickness, n is the radii ratio of R_1/R_2. The details of the deducing process can be found in Supplementary Material.

The basic thermal harvesting region was set in the center of a square domain with dimensions of 200 mm × 200 mm. And the outer radius (R_2) of the harvesting region was a constant of 60 mm for each different schemes. Furthermore, the left and right boundaries were respectively set as constant temperature boundaries with a high temperature T_L = 373 K and a low temperature T_R = 293 K to ensure a constant temperature gradient along the x direction. Finally, 293 K was adopted as the ambient temperature to reduce the effect of convection due to the temperature difference. Several schemes with different inner radii and wedge angles were developed to characterize the influence of geometrical parameters via numerical simulations based on the finite volume method.

III. GEOMETRICAL EFFECTS ON THERMAL HARVESTING BEHAVIORS

Based on the coordinate transformation[14,18,19,24] used for designing the geometrical profile of thermal harvesting devices, 6 contrasting schemes with varying R_1 and wedge angles (β) including: a. R_1 = 6.67 mm, β = 1°; b. R_1 = 12 mm, β = 1°; c. R_1 = 30 mm, β = 1°; d. R_1 = 12 mm, β = 5°; e. R_1 = 12 mm, β = 10°; and f. a bare plate of nickel steel (25% Ni) were established, and the corresponding temperature distributions for the above 6 reference schemes were obtained at 3000 s, shown in Fig. 2. The thermal harvesting behaviors is clearly observed in the central region (Part III) in the first five schemes based on the strict coordinate transformation compared with that of the bare plate. However, some non-negligible differences between the schemes are also seen in the harvesting performance in all the three parts (I, II, III). It can be seen from Figs. 2a–2c, the heat flux density in the central region (Part III) decreased with increasing R_1 owing to the reduction in the density of isothermal lines, i.e., the compressional function for the heat flux enhanced with a shrinking R_1 under similar temperature differences between the boundaries of the central regions. Furthermore, the thermal profiles corresponding to different R_1 on the interfaces of adjacent parts incurred varying perturbations, leading to discrepancies in the temperatures of test points B and C. Hence, the harvesting efficiency as calculated by Eq. (12) varied as a function of R_1.

Compared with the thermal profiles in Fig. 2b, Figures 2d and 2e respectively illustrated the temperature distributions of the schemes with β = 5° and β = 10° under R_1 = 12 mm. They clearly show that the thermal perturbations in Part I increased with increasing wedge angles, and the profiles of isothermal lines varied more smoothly in Part II with decreasing wedge angles. Hence, the temperature at the test points were expected to also be different because of the varying thermal profiles leading to changes in the harvesting behaviors that are not included in the theoretical derivation. Consequently, differences in the temperature gradient and heat flux density will also occur in Part III. Overview, different harvesting behaviors will be exhibited on varying the geometrical parameters. Therefore, to accurately evaluate and quantify the thermal perturbations of the harvesting behavior as the geometrical parameters change, two measurement lines along the y direction on the interfaces between Parts I and II (x = -0.06 m) and Parts II and III (x = -R_1 m) were selected in each of the above schemes.

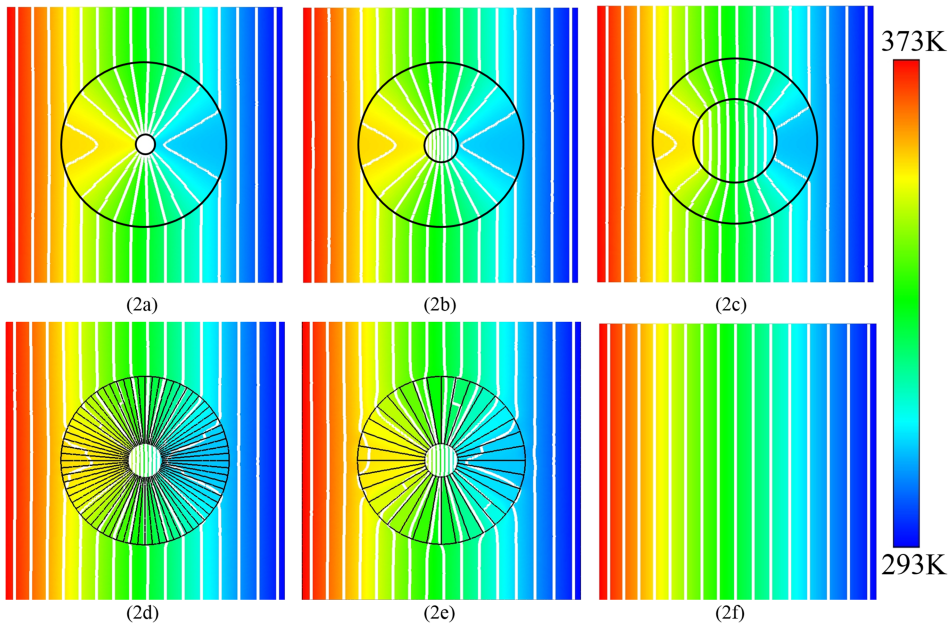

FIG. 2. Temperature distributions of the 6 thermal harvesting schemes at 3000s with varying geometrical parameters: (a) R_1 = 6.67 mm, β = 1°; (b) R_1 = 12 mm, β = 1°; (c) R_1 = 30 mm, β = 1°; (d) R_1 = 12 mm, β = 5°; (e) R_1 = 12 mm, β = 10°; (f) a bare plate of nickel steel (25% Ni).

A. The influence of the ratio of inner and outer radii

For a TO device, the deformations in the thermal profiles in Part I exhibited by the schemes and corresponding bare plates can be used to denote the perturbations outside the functional regions. This is one of the indices for evaluating the expected performance.[8,9] In general, smaller perturbations in Part I incurred less influences to ambient which should be zero deduced by Eqs. (6a) and (6b) for ideal schemes, i.e. better environmental suitability for the designed scheme. Hence, the temperature deformation[8,9] at x = -0.06 m in Part I can be written upon temperature difference as TD = $|T_{\text{scheme}}|_{x\ =\text{-}0.06\ \text{m}} - T_{\text{plate}}|_{x\ =\text{-}0.06\ \text{m}}|$, where T_{scheme} and T_{plate} represent the temperature distributions at x = -0.06 m in each harvesting schemes in Figs. 2a ~ 2e and the bare plate in Fig. 2f, respectively.

To describe the effects of the radii ratio (R_1/R_2) on Part I under $\beta = 1°$, the temperature differences between Figs. 2a ~ 2c and Fig. 2e at x = -0.06 m were illustrated in Fig. 3. It is apparent that the trend of the variation in the deformations of the thermal profiles in the first schemes with β = 1° were similar, and the slopes of the temperature differences curves were also in accordance. Moreover, most of the acute perturbations occurred in the range of -0.01–0.01 m, with the peak being located at (-0.06, 0). These perturbations were caused by the reduction in the distance of approaching Part II. That is, the anisotropy in Part II incurred fluctuations in thermal profile of the ambient temperature, approaching that of the wedge structures increasing the instability of thermal profile. Benefiting from the effective medium theory and small wedge angles, the temperature deformations and ranges of acute perturbations were small. However, the values of the deformations with varying R_1/R_2 were different. It can be seen that the values of deformations decreased with the increasing ratios of radii. That is, a smaller ratio of radii contributed to greater instability of the thermal profiles outside Part II, i.e. less influence on the surroundings.

In addition, varying R_1/R_2 also led to different effects on the thermal compression and expansion in Part II. To accurately present the deviations between the actual schemes with wedge structures in Figs. 2a ~ 2e and homogenous ideal thermal harvesting schemes under same coordinate transformations and boundaries conditions in Part II, we improved the definition of the temperature deformation[8,9] as:

$$TD = |T_{scheme}|_{x=-R_1} - T_{ideal}|_{x=-R_1}|, \tag{15}$$

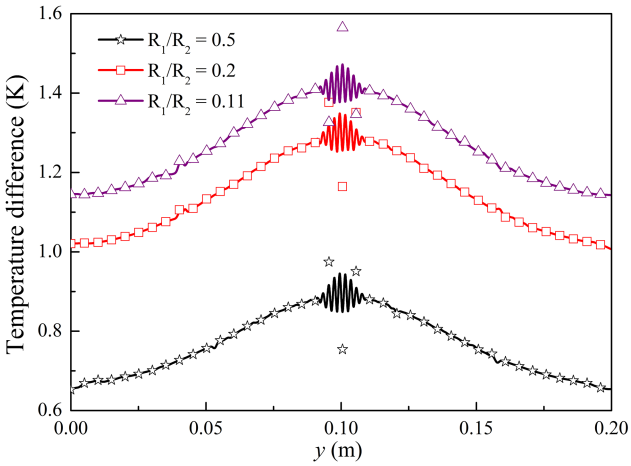

FIG. 3. Temperature differences between the bare plate and harvesting schemes with $\beta = 1^\circ$ and different R_1 at x = -0.06 m.

where, T_{scheme} denotes the temperature distributions at $x = -R_1$ in each harvesting schemes in Figs. 2a ~ 2e and T_{ideal} is the temperature distributions at $x = -R_1$ in homogenous ideal thermal harvesting schemes.

The aim of fabricating TO device is to decrease the effects on its outside and improving the expected performance simultaneously. Though the distortions of thermal flux outside the devices have been studied through the measurement lines of x = -0.06 m, the arrangements and geometrical parameters of selected materials inherently affect the thermal energy distributions in Part I and the expected performance of TO devices in Part III.[11] Whereas these conditions directly influence the thermal distributions both inside (Part III) and outside (Part I) the devices, it's essential to investigate the thermal energy perturbations inside the artificial devices through the most intuitive presentations of the thermal flux distortion along $x = -R_1$, which is beneficial to further discuss the effects of harvesting performance and to provide better understandings on the heat transfer process of the entire system. The details of the above contents were studied from the view of thermodynamics by entropy generation analysis, which can be found in Supplementary Material.

Figures 4a and 4b illustrate the temperature deformations and positions of the measurement lines ($x = -R_1$). Note that the temperatures for the ideal schemes in Part I depend on the locations of the measurement lines which should the same as those in the ideal bare plate scheme. Hence, the temperatures in Part I were different because of the variation in R_1. The temperature peaks for each schemes including the actual and homogenous ideal ones appeared at ($-R_1$, 0) shown in the upper inset of Fig. 4a, indicating that all the wedge structures with varying radii ratios in Part II played key roles in compressing the heat flux into the central regions. However, the peak intensities reduced owing to the decrease in the radii ratios both in the ideal and actual schemes in agreement with the deduction based on Eq. (9). Furthermore, the slopes of the curves in the upper inset increased with decreasing R_1/R_2, i.e., a smaller radii ratio contributes to a more significant impact on concentrating the heat flux. The lower inset in Fig. 4a shows the temperature deformations with varying R_1/R_2 calculated by Eq. (15). Clearly, the fluctuations in the thermal profiles related to the ideal schemes increased in all the parts (Parts I, II, and III) with decreasing R_1/R_2, i.e., a smaller radii ratio incurred more deviations between the ideal and actual schemes. Furthermore, the stabilizations of the *TD* in Part II rapidly reduced with decreasing R_1, particularly at ($-R_1$, 0). This indicated that more thermal energy loss occurred in actual schemes with a smaller radii ratio though it contributed to a better concentration of the heat flux.

Based on the analysis of total entropy generation in Supplementary Material, the thermal loss in Part II depends on the distribution of thermal energy. That is, a better thermodynamics process with less thermal loss requires more similar and steadier thermal distributions in both sides of the devices i.e. a better stabilization in temperature distributions. To prove the abovementioned stabilization of the thermal concentration, we performed four additional tests with varying R_1. A concept of temperature

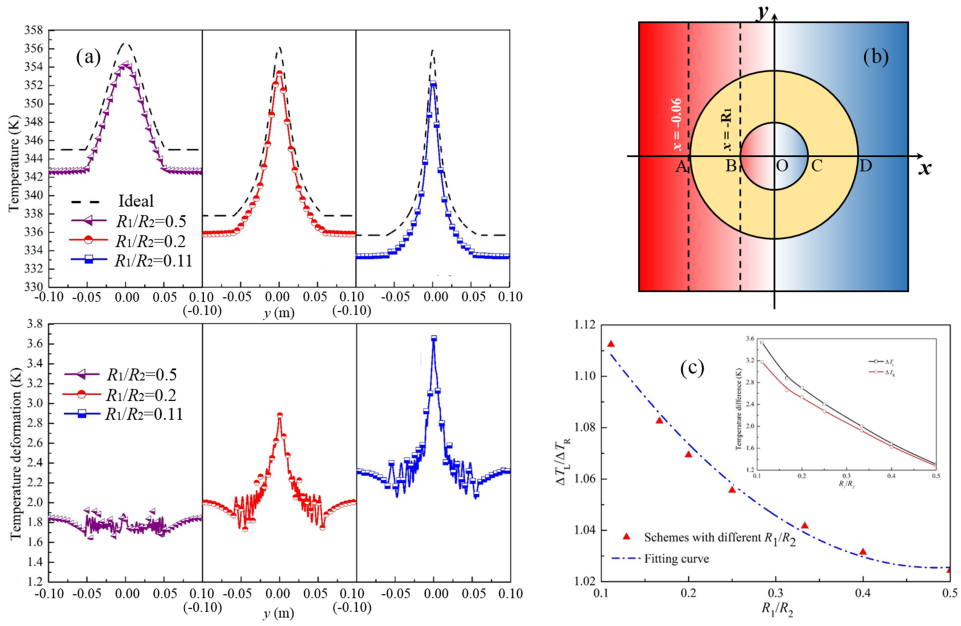

FIG. 4. Temperature deformations on the measurement lines and temperature stabilizations in Part II only with different radii ratios. (a) Temperature distributions and homologous temperature deformations on the measurement lines. (b) Positions of the measurement lines with different radii ratios. (c) Temperature stabilizations for different schemes with varying R_1/R_2; the upper inset illustrates the temperature differences between ΔT_L and ΔT_R.

stabilization with the temperature differences of the test points is proposed for the actual schemes. It can be presented as $TS = \Delta T_L/\Delta T_R$, in which $\Delta T_L = |T_A\text{-}T_B|$, and $\Delta T_R = |T_C\text{-}T_D|$. For the ideal schemes, the temperature differences of the test points can be expressed as:

$$T_A - T_B = T_C - T_D = \frac{\left(R_2 - R_1 \times \left(\frac{R_1}{R_2}\right)^{\sqrt{\varepsilon}-1}\right)(T_L - T_R)}{2x_0}, \tag{16}$$

It is easy to determine that the value of TS should be 1 for an ideal scheme. Therefore, it can be used to characterize the degree of temperature deviation and homogeneity of the energy distribution in Part II of the actual schemes. Specifically, a higher value of TS implies a larger energy deviation between the heat flux inlet and outlet regions relative to an ideal scheme, equivalent to a reduced stabilization of the thermal deviation and lower homogeneity of the energy distribution in Part II. Figure 4c presents the variation of TS with the radii ratio. The upper inset shows that the deviations between ΔT_L and ΔT_R reduced with increasing radii ratios, causing a decrease in the TS because of the lower heat loss in the smaller radii ratio schemes. In general, a harvest scheme with a larger R_1/R_2 contributed to a better stabilization and homogeneity for thermal concentration in Part II.

To further investigate the harvesting behavior in the central regions corresponding to different R_1/R_2, the central point O in Part III was selected. The conductivities in Part III were isotropic and constant; consequently, the heat flux density at the central point (0, 0) in an ideal scheme depends on the temperature gradient along the x direction, and it can be written as:

$$\nabla T_O = \frac{\partial T}{\partial x}\vec{\mathbf{n}} = \left(\frac{(T_L - T_R)}{2x_0}\left(\frac{R_1}{R_2}\right)^{\sqrt{\varepsilon}-1}\right)\vec{\mathbf{n}}, \tag{17}$$

Figure 5 illustrates the temperature gradients and homologous thermal concentration efficiencies with varying R_1/R_2. Obviously, the values of the parameters in all the original and added tests approach those of the ideal scheme (dashed line) directly calculated by Eq. (17), as shown Fig. (5a), depicting the significant effects of the radii ratios on the temperature gradient at the central point. Specifically, the temperature gradient decreased with increasing R_1/R_2. Moreover, the slope of the parameter variation reduced simultaneously with increasing R_1/R_2 owing to the property of an

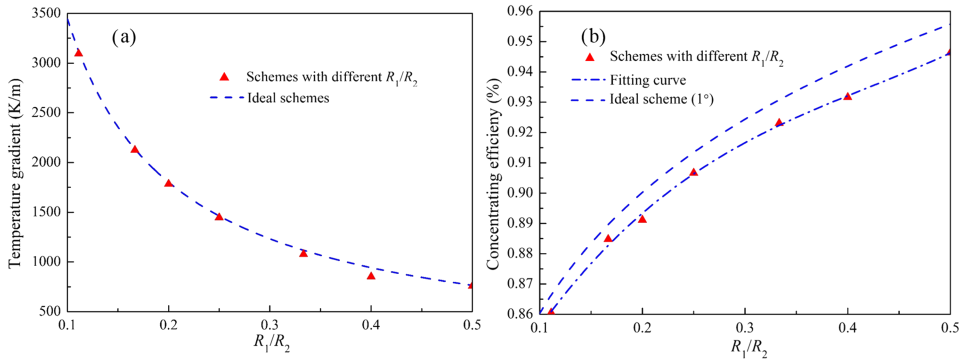

FIG. 5. Temperature gradients at central points and thermal concentrating efficiencies only with varying radii ratios. (a) Temperature gradients for all the original and added tests at (0, 0). (b) Thermal concentrating efficiencies for different schemes with varying radii ratios.

exponential function with a constant index and base less than 1. Thus, a smaller R_1/R_2 led to a better concentrating behavior because of the shorter distance. However, the concentration efficiency increased with increasing R_1/R_2, as shown in Fig. (5b), and this can also be deduced from Eq. (12). Furthermore, the efficiencies gradually diverged from the ideal values with increasing radii ratio, i.e., a harvesting scheme with a larger radii ratio ensured a higher efficiency, but with more heat loss, leading to more deviations from the ideal scheme.

In addition, the heat conduction ability and the harvesting performance were also affected by interfacial resistances. Figure 6 illustrates the variations of interface thermal resistances with the changing radii ratios. It can be seen that the interface thermal resistances reduced with the increasing radii ratio i.e. the heat conduction ability of harvesting systems enhanced by increasing the inner radii (R_1). That is, more heat transfer into the central region and less thermal loss in the artificial device. Hence, the higher concentrating efficiency can be achieved with smaller interface thermal resistances i.e. the schemes with larger radii ratios, which is in accordance with the conclusions obtained in Fig. 5. Moreover, benefiting from the reducing inner radii (R_1), the temperature gradients in the central regions increased simultaneously.

B. The influence of the wedge angle

In addition to the effects of varying the radii ratio, the angles of the wedges also affected the harvesting behavior significantly as can be seen from Figs. (2b), (2d), and (2e). Following the same methods as above, the measurement line of x = -0.06 m was selected to study the effects of the wedge angles in Part I. As shown in Fig. 7, the ranges and intensities of the fluctuations in temperature

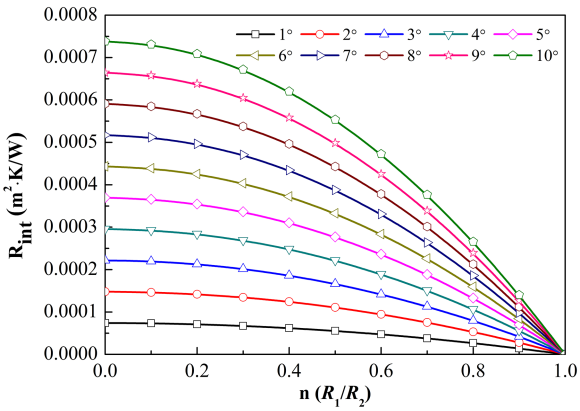

FIG. 6. The variations of interface thermal resistances with different radii ratios.

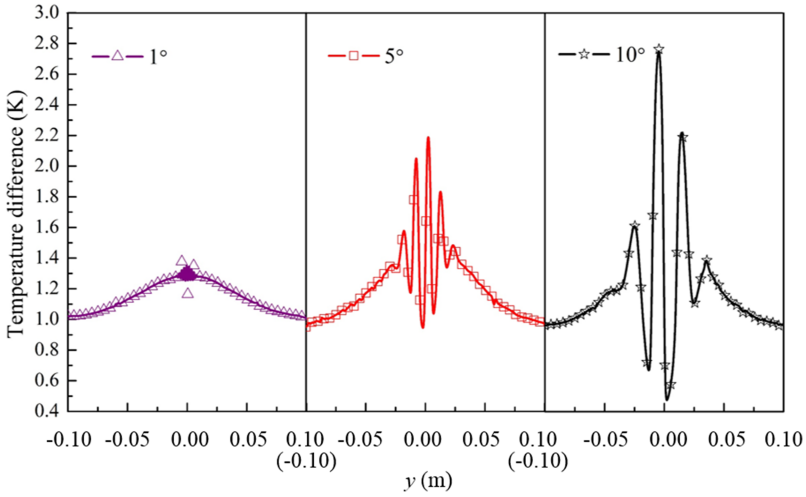

FIG. 7. Temperature differences between the bare plate and harvesting schemes with R_1 = 0.06 m and variational β at x = -0.06 m.

difference between the schemes and bare plate with the same R_1 rapidly increased with the increasing wedge angles, i.e., smaller wedge angles created higher filling rates of the two materials under certain ranges. This caused the concentrating structure in Part II to be more similar to a continuous media with pre-designed high anisotropy conductivities. Hence, the perturbations in the thermal profiles of the interfaces of Parts I and II were limited in narrower ranges of adjacent wedges with reduced wedge angles, i.e., shorter distances of heat transfer along the y direction in one wedge. In summary, smaller wedge angles contributed to more stability in the thermal profile and had less influences on the surrounding.

Similarly, the variations of the wedge angles also significantly affects the heat transfer process in Part II as shown in Fig. 8. The ideal and actual temperature profiles and their deformations are illustrated in Fig. 8a. Owing to the similarity in the radii ratios, the ideal temperature distributions were uniform. However, the peaks in the upper inset of Fig. 8a decreased and the fluctuations in the thermal profiles approaching the central points enhanced with the increasing wedge angles. In addition, the perturbations in the thermal profiles both outside and inside Part II increased. Furthermore, the fluctuations in the values of the TD calculated by Eq. (15) also drastically increased with the increasing wedge angles as shown in the lower inset of Fig. 8a. Obviously, all these deformations were caused by the varying wedge angles. The temperature profiles at x = -0.012 m in Part II should be echelonment due to the varying conductivities in adjacent wedge structure. Owing to the decreasing wedge angles, the materials became more intensive close to the central region that led to a significant reduction in the distance of the heat transfer along the y direction in one wedge, i.e., the energy fluctuations in certain ranges were assigned to more adjacent wedges with smaller angles, contributing to the smaller thermal profile perturbations. Hence, smaller wedge angles that forced the thermal profiles to be smoother, were beneficial for the neutralization of the heat fluctuations and high quality of concentration with less heat loss in Part II.

To further investigate the stabilizations of the harvesting behavior, the temperature stabilizations (TS) with varying β were examined, as shown in Fig. 8c, by conducting 3 original tests and 9 additional tests with different wedge angles of 1.5°, 2°, 2.5°, 3°, 4°, 6°, 7.5°, 8°, 9°. The values of TS increased and slope of the curve decreased with the increasing wedge values. Hence, the stabilization of the thermal harvesting behavior and homogeneity of the energy distribution also enhanced by reducing the wedge angle. In general, a smaller wedge angle not only ensured a better quality of thermal concentration, but also guaranteed a more homogeneous and steadier energy distribution in Part II. Figure 9 illustrates the temperature gradients and harvesting efficiencies at (0, 0) at a uniform radii ratio of 0.2. It is apparent that all the temperature gradients were lower than the ideal value due to the irreversible heat loss, and they linearly decrease with the increasing wedge angles as shown in Fig. 9a, i.e., a smaller wedge angle is beneficial for maintaining a higher

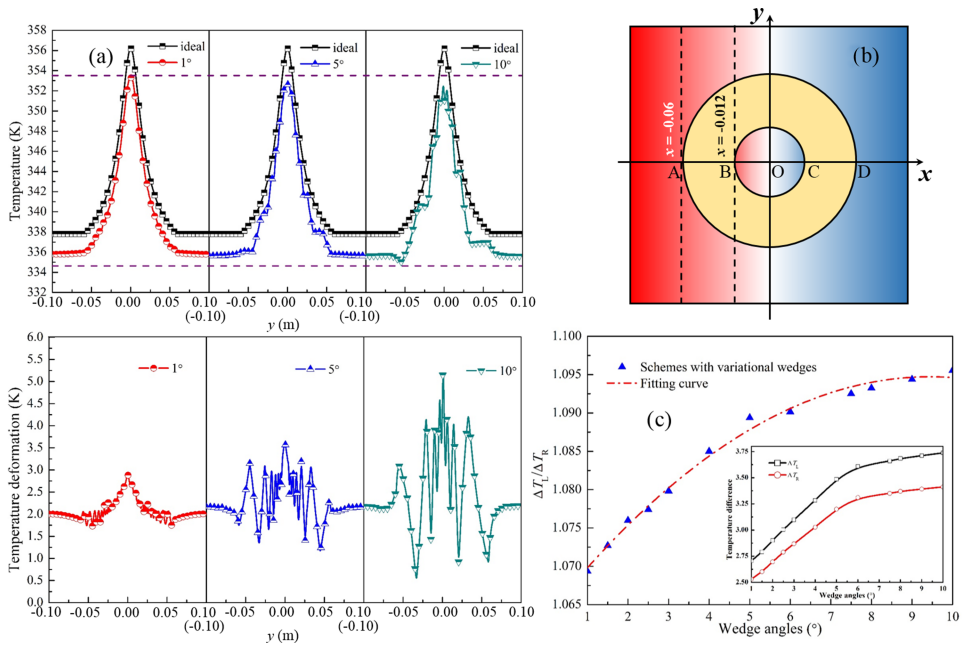

FIG. 8. Temperature deformations on the measure lines and temperature stabilizations in Part II only with different wedge angles. (a) Temperature distributions and homologous temperature deformations on the measure lines. (b) Positions of the measure lines with varying β. (c) Temperature stabilizations for different schemes with varying β, the lower inset illustrates the temperature differences between ΔT_L and ΔT_R.

temperature gradient at (0, 0), implying more thermal energy collection in Part III and less heat loss in Part II. Furthermore, the thermal concentrating efficiency also increased with the decreasing wedge angle shown in Fig. 9b, exhibiting the positive effect of a smaller wedge angle on the harvesting behavior.

Considering the effects of interfacial resistances, Figure 10 illustrates the variations of interface thermal resistances with different wedge angles. It increased linearly with the increasing wedge angle once the radii ratio was constant. That is, the heat conduction ability of harvesting system reduced with the increasing wedge angle. More thermal loss occurred on the boundaries between the interfaces and less heat transferred into the central region, which led to a lower concentrating efficiency. Hence, the findings were in accordance with those obtained in Fig. 9. Owing to the reducing wedge angles, the larger temperature gradients and higher efficiencies in the central regions were obtained simultaneously.

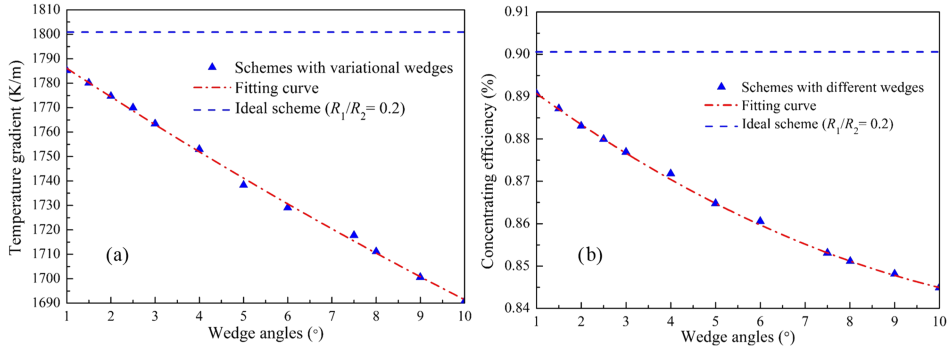

FIG. 9. Temperature gradients at central points and thermal concentrating efficiencies only with varying wedge angles. (a) Temperature gradients for all the original and added tests at (0, 0). (b) Thermal concentrating efficiencies for different schemes with varying wedge angles.

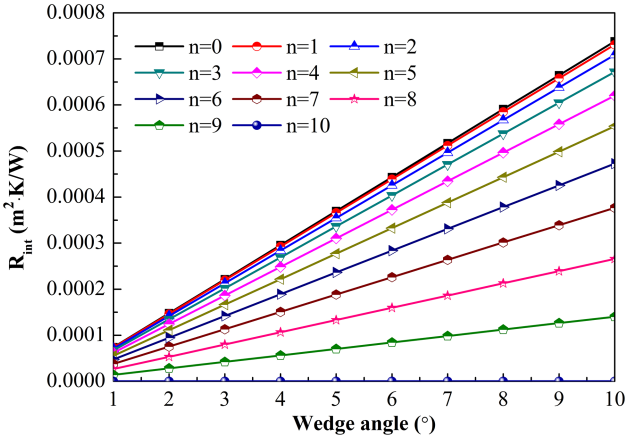

FIG. 10. The variations of interface thermal resistances with different wedge angles.

Overall, the temperature gradients in Part III increased with the decreasing ratio of R_1/R_2. Furthermore, the harvesting efficiency improved with the smaller wedge angles and larger radii ratio benefiting from the decreasing of interface thermal resistances and the increasing of continuous media. In addition, the heat conduction ability of Part II increased with reducing interface thermal resistances. That is, it's an effective way to employ small wedge angles in the interfacial material layers and appropriate radii ratios for fabricating satisfied harvesting devices. Whereas the different requirements of thermal concentration under certain materials are demanded in varying potential applications such as thermoelectricity, solar collectors, heat storage and fuel cells, an appropriate structure considering the related limitations of the radii and wedge elements should be adopted through adjusting geometrical parameters. Hence, the above investigations serve for achieving the quantitative discussions on the harvesting performance and related structural parameters, in order to provide references on fabricating the best-fit concentrating devices in potential applications.

C. Modified harvesting efficiency considering the effects of wedge structure

Considering the effects of the radii ratios and wedge angles, the actual concentrating efficiencies could not achieve the ideal values, as evidenced in Figs. 5b and 9b. Hence, we propose a modified efficiency to evaluate the wedge structure-based[14–20,22–24] concentration devices based on the fitting efficiency curves of the test findings. Excluding the influence of convection by employing a vacuum chamber,[39] the modified efficiency for the selected materials can be presented as:

$$\eta = \left(\frac{R_1}{R_2}\right)^c = \left(\frac{R_1}{R_2}\right)^{\left(0.92468+0.07774\times\frac{\beta}{\beta_0}-0.002424\times\left(\frac{\beta}{\beta_0}\right)^2\right)\left(\sqrt{\varepsilon}-0.00107+0.03023\times\frac{R_1}{R_2}\right)}, \quad (18)$$

where, β_0 denotes the standard angle fixed at 1°, c is the modified coefficient which can also replace $\sqrt{\varepsilon}$ appeared in the abovementioned expressions. Equation (18) indicates the approximate relationships between the harvesting efficiencies and homologous design parameters including the wedge angles

TABLE I. Results of confirmation tests and homologous errors.

	Design parameters			Harvesting efficiency		
Tests	Radii ratio (R_2/R_1)	Wedge angle (°)	Conductivities ($W\cdot m^{-1}\cdot K^{-1}$) and ratios ($\kappa_\theta/\kappa_r$)	Predicted values	Actual values	Error (%)
1	9	3	0.00426 (κ_A=398, κ_B = 0.425)	0.84477	0.841987	0.331%
2	6	4.5	0.01206 (κ_A=236, κ_B = 0.716)	0.77990	0.78425	-0.683%
3[17,34]	5	3.6	0.002714 (κ_A=398, κ_B = 0.27)	0.89785	0.88459[34]	1.500%
4[18]	4	5	0.001521 (κ_A=394, κ_B = 0.15)	0.91513	0.90810	0.774%
5[21]	5	10	0.002528 (κ_A=237, κ_B = 0.15)	0.87825	0.85410	2.828%

and ratios of the conductivities and radii. This is in agreement with the theoretical values in that the maximum possible efficiency satisfied the result calculated by Eq. (12) if the material in Part II is a continuous media with pre-designed conductivity components in different directions. Furthermore, five confirmation tests including 2 random schemes and 3 results of finally fabricated devices[34] based on previous researches[17,18,21] were conducted to verify the accuracy of modified efficiency. The results are shown in Table I. All the results calculated by Eq. (18) approached the measurement confirmed values, and the highest error was 2.828%, indicating the accuracy of the modification efficiency.

IV. CONCLUSION

In this paper, the geometrical effects of the radii ratios and wedge angles on the concentrating behavior were investigated. Our findings revealed that smaller radii ratios contributed to a better heat flux concentration in Part III However, they simultaneously increased interface thermal resistances and destabilized the heat distributions in Part II, and generated stronger perturbations in thermal profiles both in Parts I and II, leading to a greater heat loss and lower thermal concentrating efficiency of the entire system. Moreover, the smaller wedge angle ensured a higher temperature gradient in Part III and less interface thermal resistances in Part II. In addition, Part II behaved similar to a continuous media that led to a more uniform heat distribution as a consequence. In general, the thermal profiles perturbations significantly reduced and homologous efficiency enhanced. Furthermore, the perturbations of the temperature differences decreased in Part I with the reducing wedge angles, indicating better environmental suitability. Finally, a modification of the harvesting efficiency for the wedge structure schemes was proposed considering the varying wedge angles, ratios of radii, and conductivities, and it exhibited reasonable accuracy as proven by confirmation tests. Furthermore, it can provide quantitative discussions of the influences of such geometrical parameters on the concentrating performances based on the detailed investigations on the radii ratios and wedge angles. The findings are useful for achieving thermal concentration with a high efficiency, and they serve as a guide for the enhancement of efficient heat focus that has several potential applications in novel heat storage, thermal sensors, solar cells, and thermoelectric devices. In addition, this work can be also available in reference to achieving high-efficiency focus in the electromagnetic field.

SUPPLEMENTARY MATERIAL

See Supplementary Material for the details of Eq. (14) and related entropy generation analysis of the entire system.

ACKNOWLEDGMENTS

This work was supported by the National Natural Science Foundation of China (Grant Nos. 51776050 and 51536001).

[1] J. B. Pendry, D. Schurig, and D. R. Smith, Science **312**, 1780 (2006).
[2] J. Valentine, J. Li, T. Zentgraf, G. Bartal, and X. Zhang, Nat. Mater. **8**, 568 (2009).
[3] W. X. Jiang, D. Bao, and T. J. Cui, J. Opt. **18**, 044022 (2016).
[4] D. Schurig, J. J. Mock, B. J. Justice, S. A. Cummer, J. B. Pendry, A. F. Starr, and D. R. Smith, Science **314**, 977 (2006).
[5] Q. Li and J. S. Vipperman, Appl. Phys. Lett. **105**, 101906 (2014).
[6] T. Bückmann, M. Thiel, M. Kadic, R. Schittny, and M. Wegener, Nat. Commun. **5**, 4130 (2014).
[7] R. Schittny, M. Kadic, S. Guenneau, and M. Wegener, Phys. Rev. Lett. **110**, 195901 (2013).
[8] T. Han, T. Yuan, B. Li, and C. W. Qiu, Sci. Rep. **3**, 1593 (2013).
[9] T. Han, X. Bai, D. Gao, J. T. L. Thong, B. Li, and C. W. Qiu, Phys. Rev. Lett. **112**, 054302 (2014).
[10] G. Q. Xu and H. C. Zhang, AIP Adv. **6**, 095107 (2016).
[11] G. Q. Xu, H. C. Zhang, Q. Zou, and Y. Jin, Int. J. Heat Mass Trans. **109**, 746 (2017).
[12] Y. Ma, L. Lan, W. Jiang, F. Sun, and S. He, NPG Asia Mater. **5**, e73 (2013).
[13] Y. Ma, Y. Liu, M. Raza, Y. Wang, and S. He, Phys. Rev. Lett. **113**, 205501 (2014).
[14] S. Guenneau, C. Amra, and D. Veynante, Opt. Express **20**, 8207 (2012).
[15] R. Hu, X. Wei, J. Hu, and X. Luo, Sci. Rep. **4**, 3600 (2014).
[16] T. Han, J. Zhao, T. Yuan, D. Y. Lei, B. Li, and C. W. Qiu, Energy Environ. Sci. **6**, 3537 (2013).
[17] F. Chen and D. Y. Lei, Sci. Rep. **5**, 11552 (2015).
[18] T. Han, X. Bai, D. Liu, D. Gao, B. Li, J. T. L. Thong, and C. W. Qiu, Sci. Rep. **5**, 10242 (2015).

[19] X. Shen, Y. Li, C. Jiang, Y. Ni, and J. Huang, Appl. Phys. Lett. **109**, 031907 (2016).
[20] M. Moccia, G. Castaldi, S. Savo, Y. Sato, and V. Galdi, Phys. Rev. X **4**, 021025 (2014).
[21] C. Lan, B. Li, and J. Zhou, Opt. Express **23**, 24475 (2015).
[22] C. Lan, K. Bi, X. Fu, B. Li, and J. Zhou, Opt. Express **24**, 23072 (2016).
[23] C. Lan, M. Lei, K. Bi, B. Li, and J. Zhou, Opt. Express **24**, 29537 (2016).
[24] T. Chen, C. N. Weng, and Y. L. Tsai, J. Appl. Phys. **117**, 054904 (2015).
[25] Y. Liu, W. Jiang, S. He, and Y. Ma, Opt. Express **22**, 170006 (2014).
[26] S. Narayana and Y. Sato, Phys. Rev. Lett. **108**, 214303 (2012).
[27] X. He and L. Wu, Appl. Phys. Lett. **105**, 221904 (2014).
[28] Y. Li, X. Shen, J. Huang, Y. Chen, Y. Ni, and J. Huang, Phys. Rev. Lett. **115**, 195503 (2015).
[29] D. Jiang, W. Yang, and A. Tang, Energy Convers. Manage. **103**, 359 (2015).
[30] W. Zhang, L. Yang, and H. Zhang, S. You, and C. Zhu, Energy Convers. Manage. **129**, 11 (2016).
[31] Z. Khan, Z. Khan, and A. Ghafoor, Energy Convers. Manage. **115**, 132 (2016).
[32] H. Heidary, M. J. Kermani, and B. Dabir, Energy Convers. Manage. **124**, 51 (2016).
[33] X. Shen, C. Jiang, Y. Li, and J. Huang, Appl. Phys. Lett. **109**, 201906 (2016).
[34] G. Park, S. Kang, H. Lee, and W. Choi, Sci. Rep. **7**, 41000 (2017).
[35] G. Q. Xu, H. C. Zhang, Y. Jin, S. Li, and Y. Li, Opt. Express **25**, A419 (2017).
[36] F. M. Canbazoglu, K. P. Vemuri, and P. R. Bandaru, Appl. Phys. Lett. **106**, 143904 (2015).
[37] B. W. Kim, S. H. Park, R. S. Kapadia, and P. R. Bandaru, Appl. Phys. Lett. **102**, 243105 (2013).
[38] R. S. Prasher, J. Heat Trans. **123**(5), 969 (2001).
[39] R. Hu, S. Zhou, X. Yu, and X. Luo, J. Phys. D. Appl. Phys. **49**, 415302 (2016).